ROYAL SOCIETY
OF CHEMISTRY

PAPER

Check for updates

Strategic design of triphenylamine- and triphenyltriazine-based two-dimensional covalent organic frameworks for CO_2 uptake and energy storage†

Ahmed F. M. EL-Mahdy,[ab] Cheng-Han Kuo,[a] Abdulmohsen Alshehri,[c] Christine Young,[d] Yusuke Yamauchi, [iD][ef] Jeonghun Kim [iD] *[e] and Shiao-Wei Kuo [iD] *[a]

Hexagonally ordered covalent organic frameworks (COFs) are interesting new crystalline porous materials that have massive potential for application in gas storage. Herein, we report the synthesis of two series of two-dimensional hexagonally ordered COFs—TPA-COFs and TPT-COFs—through one-pot polycondensations of tris(4-aminophenyl)amine (TPA-3NH$_2$) and 2,4,6-tris(4-aminophenyl)triazine (TPT-3NH$_2$), respectively, with triarylaldehydes featuring different degrees of planarity, symmetry, and nitrogen content. All the synthesized COFs exhibited high crystallinity, large BET surface areas (up to 1747 m^2 g^{-1}), excellent thermal stability, and pore size distributions from 1.80 to 2.55 nm. The symmetry and planarity of the monomers strongly affected the degrees of crystallinity and the BET surface areas of the resultant COFs. In addition, these COFs displayed excellent CO_2 uptake efficiencies of up to 65.65 and 92.38 mg g^{-1} at 298 and 273 K, respectively. The incorporation of the more planar and higher-nitrogen-content triaryltriazine unit into the backbones of the TPA-COFs and TPT-COFs enhanced the interactions with CO_2, leading to higher CO_2 uptakes. Moreover, the synthesized COFs exhibited electrochemical properties because of their conjugated structures containing redox-active triphenylamine groups. This study exposes the importance of considering the symmetry and planarity of the monomers when designing highly crystalline COFs; indeed, the structures of COFs can be tailored to vary their functionalities for specific applications.

Introduction

The past few years have witnessed the synthesis of various collections of covalent organic frameworks (COFs).[1–3] These covalently bonded frameworks are porous organic materials that have light weight, highly crystalline, and highly porous; most importantly, however, their chemical structures can be designed and modified using organic synthesis to ensure desired functions. Thus, they have garnered great attention for their diverse

[a]Department of Materials and Optoelectronic Science, National Sun Yat-Sen University, Kaohsiung 80424, Taiwan. E-mail: kuosw@faculty.nsysu.edu.tw

[b]Chemistry Department, Faculty of Science, Assiut University, Assiut 71516, Egypt

[c]Department of Chemistry, King Abdulaziz University, P.O. Box. 80203, Jeddah 21589, Saudi Arabia

[d]International Centre for Materials Nanoarchitectonics (MANA), National Institute for Materials Science (NIMS), 1-1 Namiki, Tsukuba, Ibaraki 305-0044, Japan

[e]School of Chemical Engineering and Australian Institute for Bioengineering and Nanotechnology (AIBN), The University of Queensland, Brisbane, QLD 4072, Australia. E-mail: jeonghun.kim@uq.edu.au

[f]Department of Plant & Environmental New Resources, Kyung Hee University, 1732 Deogyeong-daero, Giheung-gu, Yongin-si, Gyeonggi-do 446-701, South Korea

† Electronic supplementary information (ESI) available: Details of synthetic approaches, and materials characterization. See DOI: 10.1039/c8ta04781b

application in gas storage and separation,[4–7] chemical sensing,[8–11] catalysis,[12–16] membrane separation,[17] environmental remediation,[18] energy storage,[19–22] drug delivery,[23–25] and electronic devices.[26] The discovery of new covalent bonds suitable for the construction of highly crystalline organic frameworks remains a challenge. Reported methods for the construction of COFs have depended on the formation of strong covalent bonds through a reversible condensation strategy using, for example, boronic ester formation,[27,28] Schiff base (imine) condensation of aromatic amines and aromatic aldehydes,[29–31] triazine polymerization,[32,33] and azodioxide formation.[34] Among these approaches, imine condensation has been particularly widely used for the synthesis of various COFs having a range of crystallinities and porosities, mainly because of the high stability of imino bonds and the wide availability of monomers containing aldehyde and amino functional groups.[35,36]

One of the greatest attractions of COFs is that their structures can be controlled by varying their organic monomers.[37,38] Nevertheless, controlling the crystallinity and porosity of a COF remains challenging.[39] Previous reports have suggested that the porosity and crystallinity of COFs can be enhanced through the use of three methods. First, the crystallinity of COFs has been

improved by controlling the layer interactions and layer planarity through the introduction of hydrogen bonds.[40] Second, strong π-stacking between the intralayers of the COFs has generated highly crystalline and porous COFs.[41] Third, the crystallinity of COFs has been controlled by adjusting the rigidity or flexibility of the monomers. For example, Bein *et al.*[42] and Banerjee *et al.*[43] discovered that flexible molecular docking sites and monomer planarity played important roles in determining the porosity and crystallinity of the resulting COFs.
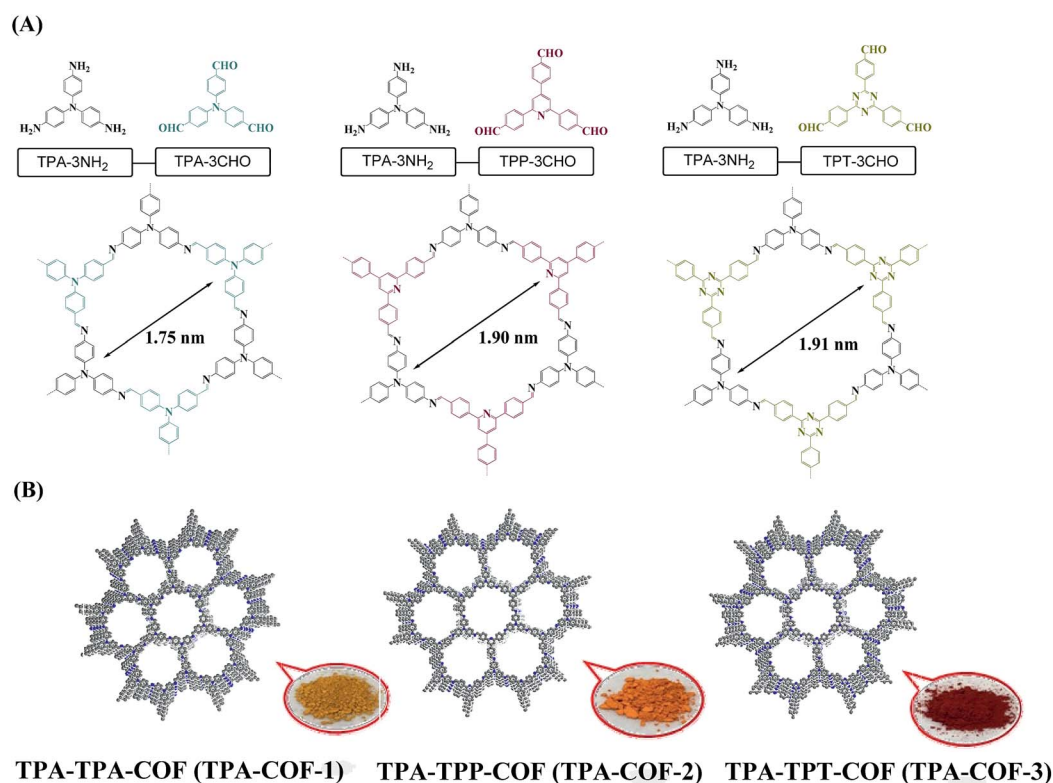
Previously, COFs having symmetrical monomer units in their hexagonal structure have been constructed by other researchers. Loh *et al.* described the utilization of symmetrical monomers tetrakis(4-formylphenyl)ethane and tetrakis(4-aminophenyl) ethane for the construction of 2D-COFs.[44] In addition, Lotsch *et al.* reported the synthesis of TTI-COFs through the imine-condensation of two symmetric monomers tris(4-formylphenyl) triazine and tris(4-aminophenyl)triazine.[45] Furthermore, Jiang *et al.* also reported the utilization of symmetrical monomers tris(4-aminophenyl)amine and tris(4-formylphenyl)amine for the synthesis of TFPA–TAPA-COFs, and tris(4-formylphenyl) benzene (TFPB) and tris(4-aminophenyl)benzene (TAPB) for TFPB–TAPB-COFs.[46]

Although the examples above confirmed the crystallinity of COFs, these structures have limited application in gas storage or electrochemical energy storage; furthermore, a few previous reports have described the influence of both the symmetry and planarity of the monomers together on the properties and applications of the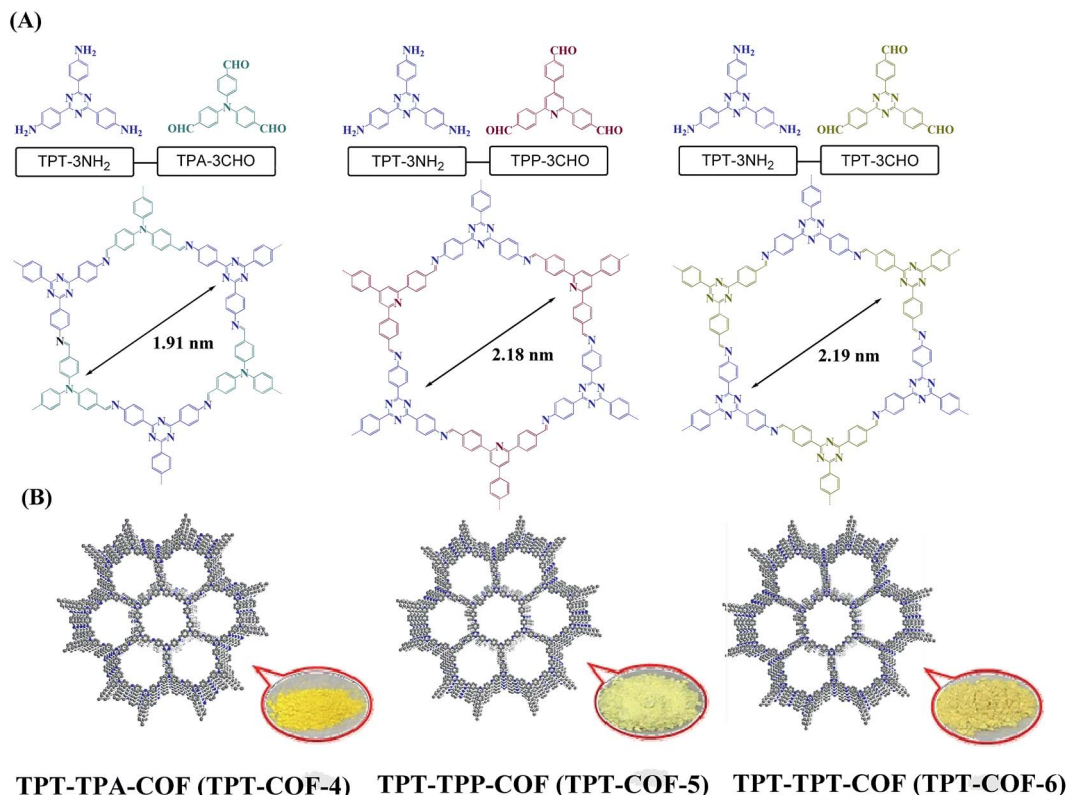 resultant COFs. Thus, in this present study, we investigated the ability to control the crystallinity of COFs as well as its effect on the uptake of carbon dioxide (CO_2). We designed two series of isoreticular two-dimensional (2D) COFs—TPA-COFs and TPT-COFs, having the same hexagonal topology—through one-pot polycyclocondensation of tris(4-aminophenyl)amine (TPA-3NH$_2$) and 2,4,6-tris(4-aminophenyl)triazine (TPT-3NH$_2$), respectively, as triarylamine monomers, and three triarylaldehyde monomers having different degrees of planarity, tris(4-formylphenyl)amine (TPA-3CHO), 2,4,6-tris(4-formylphenyl) pyridine (TPP-3CHO), and 2,4,6-tris(4-formylphenyl)triazine (TPT-3CHO), as displayed in Schemes 1 and 2.

Results and discussion

To investigate the effects of the planarity and symmetry of the monomers on the porosity and crystallinity of the COFs and their application in CO_2 capture, we synthesized TPA-COFs and TPT-COFs through the reactions of TPA-3NH$_2$ (Fig. S1–S4 and S17†) and TPT-3NH$_2$ (Fig. S5, S6 and S18†), respectively, as flexible triarylamine monomers, with TPA-3CHO (Fig. S7, S8 and S19†), TPP-3CHO (Fig. S9–S12 and S20†) and TPT-3CHO (Fig. S13–S16 and S21†) as flexible triarylaldehyde monomers. As listed in Table 1, TPT-3NH$_2$ is more planar than TPA-3NH$_2$, and TPT-3CHO is more planar than TPP-3CHO and TPA-3CHO. The TPA-COF series of compounds were produced under solvothermal conditions through one-pot polycondensations between TPA-3NH$_2$ and TPA-3CHO, TPP-3CHO, and TPT-3CHO, in mesitylene/dioxane (1 : 1) containing acetic acid as a catalyst,

(A)

TPA-3NH$_2$ — TPA-3CHO   1.75 nm

TPA-3NH$_2$ — TPP-3CHO   1.90 nm

TPA-3NH$_2$ — TPT-3CHO   1.91 nm

(B)

TPA-TPA-COF (TPA-COF-1)   **TPA-TPP-COF (TPA-COF-2)**   **TPA-TPT-COF (TPA-COF-3)**

Scheme 1 (A) Schematic strategies for the synthesis of three isoreticular 2D TPA-COFs from triphenylamine with three aldehyde monomers of various planarities. (B) 2D Simulation of TPA-COFs. Color code: C, gray; N, blue.
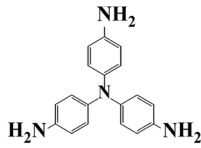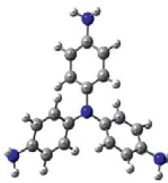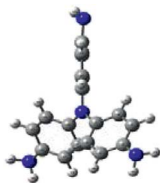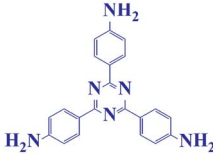
This journal is © The Royal Society of Chemistry 2018

J. Mater. Chem. A, 2018, **6**, 19532–19541 | **19533**
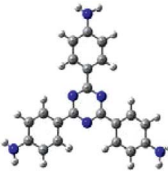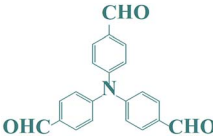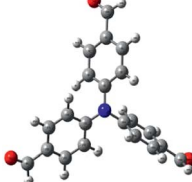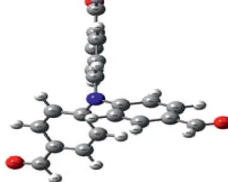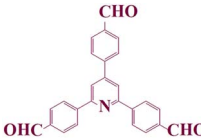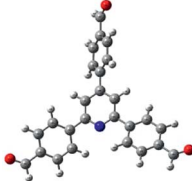
Scheme 2 (A) Schematic strategies for the synthesis of three isoreticular 2D TPT-COFs from triphenyl triazine with three aldehyde monomers of different planarities and (B) 2D-simulation of TPT-COFs. C: gray, N: blue.

at 120 °C for 4 days to yield a TPA–TPA-COF (TPA-COF-1, 87% yield), TPA–TPP-COF (TPA-COF-2, 85%), and TPA–TPT-COF (TPA-COF-3, 88%), respectively (Scheme 1). Similarly, the TPT-COF series of compounds were also obtained through one-pot polycondensations between TPT-3NH$_2$ and TPA-3CHO, TPP-3CHO, and TPT-3CHO to give a TPT–TPA-COF (TPT-COF-4, 82%), TPT–TPP-COF (TPT-COF-5, 86%), and TPT–TPT-COF (TPT-COF-6, 89%), respectively (Scheme 2). The synthesized TPA-COFs and TPT-COFs were insoluble in common organic solvents, including acetone, *N,N*-dimethylformamide, dimethylsulfoxide, tetrahydrofuran, and dioxane.
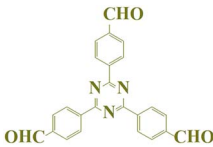
The success of the polycondensations yielding the COFs was confirmed using Fourier transform infrared (FTIR) spectroscopy, elemental analysis, and solid state ^{13}C CP MAS NMR spectroscopy. In the FTIR spectra, the triarylamine monomers were characterized by signals at 3460–3207 cm^{-1} for the NH$_2$ groups and 1579–1504 cm^{-1} for the aromatic C=C groups, while the triarylaldehyde monomers were characterized by signals at 1706–1693 cm^{-1} for the C=O groups and 1598–1504 cm^{-1} for the aromatic C=C groups (Fig. S22–S27†). For more convenience, we focused on the functionalized NH$_2$ and C=O groups. After poly-condensations, the FTIR spectra of the TPA-COFs and TPT-COFs revealed the almost complete disappearance of the signals for the NH$_2$ and C=O units of the monomers, and the appearance of strong signals at 1627–1616 cm^{-1} representing the C=N stretching vibrations,[44–46] suggesting the formation of the COFs through Schiff-base polycondensations. The terminal NH$_2$ and C=O groups on

the surface of the resultant COFs appeared as weak signals at 3475–3380 and 1703–1697 cm^{-1}, respectively. Elemental analysis results of the TPA-COFs and TPT-COFs were consistent with the theoretical values for their 2D sheets (Table S1†). Solid state ^{13}C NMR spectroscopy was further utilized to confirm the formation of TPA-COFs and TPT-COFs. As shown in Fig. S4, S6, S8, S12, and S16,† the ^{13}C NMR spectra of the triarylamine monomers exhibited a signal at 154–143 ppm for the carbon atom attached to the amino (C-NH$_2$) group, while the triarylaldehyde monomers exhibited a strong signal at 193–191 ppm for the aldehyde carbonyl C=O group. In addition, the ^{13}C NMR spectra of the TPT-3NH$_2$ and TPT-3CHO monomers showed a massive peak at 170 and 171 ppm for the triazine core, respectively. After polycondensations, the solid state ^{13}C NMR spectra of TPA-COFs and TPT-COFs were characterized by the disappearance of the aldehyde carbonyl C=O group and the appearance of single main peaks at around 161 ppm for the TPA-COFs and at around 164 ppm for the TPT-COFs, attributable to the resonances of the imino C=N carbon nuclei in the six COFs.[44,47] In addition, the ^{13}C NMR spectra of the triazine-containing COFs featured a downfield shift of the triazine core of around 176 ppm (Fig. 1). Furthermore, thermogravimetric analysis (TGA) of the TPA-COFs and TPT-COFs revealed that these six COFs are thermally stable up to 510–574 °C (Fig. S28, Table S2†). Using the temperature of 10% weight loss (T_{d10}) and the onset temperature (T_{onset}) as standards, we found that the TPT–TPT-COF (TPT-COF-6) was the most thermally stable of our COFs, with a value of T_{d10} of 574 °C, a value of

19534 | *J. Mater. Chem. A*, 2018, **6**, 19532–19541

This journal is © The Royal Society of Chemistry 2018

Table 1 DFT geometry optimization of the monomers, using the B3LYP/6-311G(d,p) method

Monomer name	Chemical structure	3D-front view	3D-side view	Torsion
TPA-3NH$_2$				−35.44
TPT-3NH$_2$				0
TPA-3CHO				−30.84
TPP-3CHO				3.77
TPT-3CHO				0

T_{onset} of 554 °C and a char yield of 61%, while the TPA–TPA-COF (TPA-COF-1) was the most thermally unstable COF with a value of T_{d10} of 510 °C, a value of T_{onset} of 475 °C and a char yield of 58%; for the TPA–TPP-COF (TPA-COF-2), TPA–TPT-COF (TPA-COF-3), TPT–TPA-COF (TPT-COF-4), and TPT–TPP-COF (TPT-COF-5), the values of T_{d10} were 520, 531, 549, and 553 °C, respectively, and the char yields were 67, 58, 55, and 49%, respectively. Moreover, the TPA–TPP-COF (TPA-COF-2), TPA–TPT-COF (TPA-COF-3), TPT–TPA-COF (TPT-COF-4), and TPT–TPP-COF (TPT-COF-5) showed values of T_{onset} of 485, 503, 539, and 541 °C, respectively. Thus, the symmetry and planarity of the monomers highly affect the thermal stability. For the symmetrical monomers, the presence of the symmetrical and most planar TPT-3NH$_2$ and TPT-3CHO monomers together in the same COF (TPT-COF-6) largely enhanced the thermal stability, while the presence of the symmetrical and least planar TPA-3NH$_2$ and TPA-3CHO monomers together in the same COF (TPA-COF-1) largely decreased the thermal stability. On the other hand, for the unsymmetrical monomers, incorporation of

the planar monomer appeared to increase the thermal stability of the resultant COFs; The TPA–TPT-COF (TPA-COF-3) is more thermally stable than the TPA–TPP-COF (TPA-COF-2), and the TPT–TPP-COF (TPT-COF-5) is more thermally stable than the TPT–TPA-COF (TPT-COF-4).

We studied the crystal structures of the TPA-COFs and TPT-COFs using powder X-ray diffraction (PXRD) in combination with computational simulations. As displayed in Fig. 2A, the PXRD patterns of the TPA-COFs confirmed the formation of crystalline frameworks having periodic hexagonal 2D honeycomb-type lattices. The structure of the TPA–TPA-COF (TPA-COF-1) was characterized by a sharp diffraction peak at a value of 2θ of 5.05°, corresponding to a (100) reflection, in addition to two other peaks at 9.15 and 13.66°, which were assigned to (210) and (310) reflections, respectively. We attribute the slightly broad peak at a value of 2θ of 20.25° to the (100) reflection caused by π-stacking between the COF layers. The TPA–TPP-COF (TPA-COF-2) also exhibited PXRD peaks at values of 2θ of 4.63, 8.11, 12.19, and 21.10°, attributed to the (100),
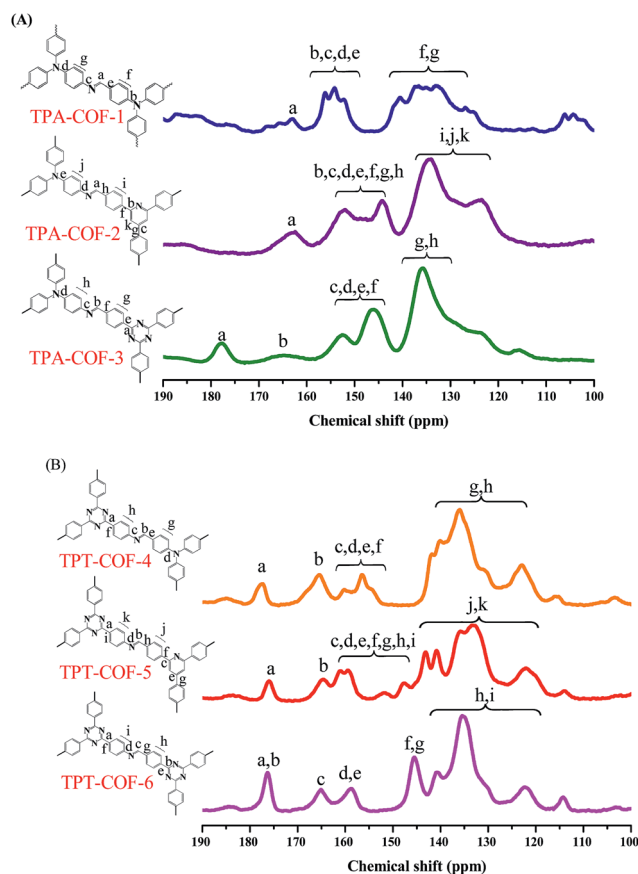
Fig. 1 Solid state ^{13}C CP MAS NMR spectra of (A) TPA-COFs: TPA–TPA-COF (TPA-COF-1), TPA–TPP-COF (TPA-COF-2), and TPA–TPT-COF (TPA-COF-3), and (B) TPT-COFs: TPT–TPA-COF (TPT-COF-4), TPT–TPP-COF (TPT-COF-5), and TPT–TPT-COF (TPT-COF-6).
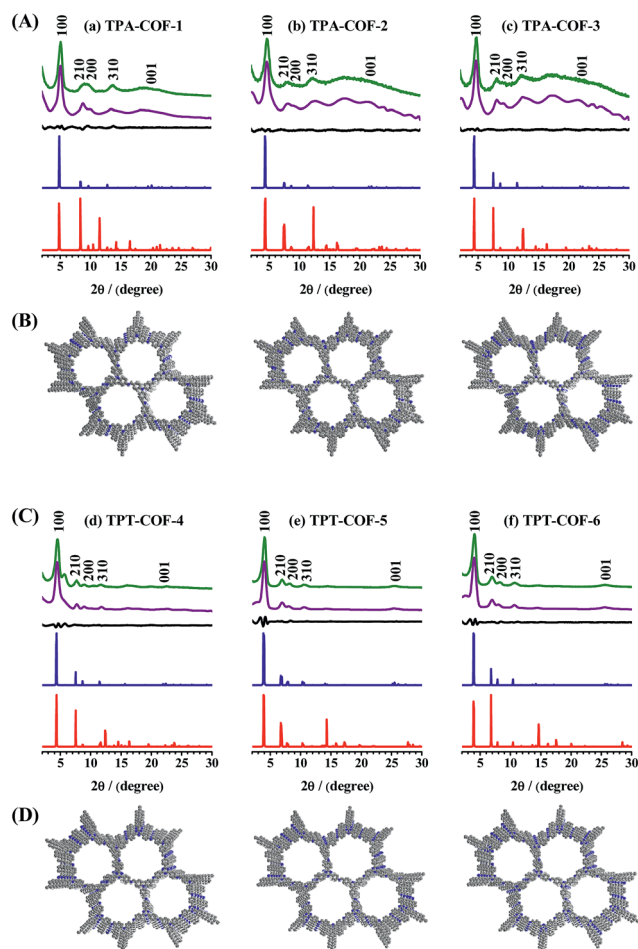

Fig. 2 (A and C) PXRD patterns of the (A) TPA-COFs and (C) TPT-COFs (green for the experimentally observed) compared with the simulated patterns calculated for the Rietveld refinement (purple), their difference (black), AA-stacking (blue), and AB-stacking (red). (B and D) Views of space-filling models of the (B) TPA-COFs and (D) TPT-COFs along the AA-stacking crystal structures (color code: C, gray; N, blue).

(210), (310), and (001) reflections, respectively. Furthermore, the TPA–TPT-COF (TPA-COF-3) exhibited its main PXRD peak at a value of 2θ of 4.62°, corresponding to the (100) reflection, as well as four other peaks at 5.83, 8.07, 12.35, and 21.25°, that we assign to the (210), (200), (310), and (001) reflections, respectively. In addition, we calculated the average d-spacings between the 100 planes (d_{100}) and the interlayer distances between the 2D sheets of planes, according to the Bragg equation, $n\lambda = 2d \sin \theta$, where n is an integer (here, $n = 1$) and λ is the wavelength of the incident waves (here, $\lambda = 0.154$ nm). For the TPA–TPA-COF (TPA-COF-1), TPA–TPP-COF (TPA-COF-2), and TPA–TPT-COF (TPA-COF-3), the values of d_{100} were 1.75, 1.90, and 1.91 nm, respectively, and their inter-layer distances were 4.40, 4.21, and 4.20 Å, respectively (Table 2). The TPT-COFs also possessed periodic hexagonal 2D honeycomb-type frameworks (Fig. 2C). The TPT–TPA-COF (TPT-COF-4) exhibited PXRD diffraction peaks at values of 2θ of 4.62, 5.58, 7.75, 10.35, and 25.45°, which we assigned to the (100), (210), (200), (310), and (001) reflections, respectively. The TPT–TPP-COF (TPT-COF-5) provided PXRD peaks at values of 2θ of 4.05, 6.29, 8.18, 10.60, and 25.48°, attributable to the (100), (210), (200), (310), and (001) reflections, respectively. Finally, the TPT–TPT-COF (TPT-COF-6) displayed its main PXRD peak at a value of 2θ of 4.04°, corresponding to the (100) reflection, as well as four other peaks

at 6.97, 8.23, 10.67, and 25.56°, which we assign to the (210), (200), (310) and (001) reflections, respectively. The TPT-COF-4, TPT-COF-5, and TPT-COF-6 featured values of d_{100} of 1.91, 2.18, and 2.19 nm, and interlayer distances of 3.50, 3.49, and 3.48 Å, respectively (Table 2).

The experimental PXRD reflections of the TPA-COFs and TPT-COFs matched well with their theoretical patterns (Fig. 2A and C, purple curves), as evidenced by negligible differences (Fig. 2A and C, black curves) obtained from the structural simulations of the AA-eclipsed layer stacking modes (Tables S3–S8, Fig. S29†). Interestingly, these results suggested that the level of planarity in the precursor monomer strongly affected the crystallinity of the resulting COF. By increasing the planarity of the monomers, the value of d_{100} increased and the interlayer distance decreased. It has previously been reported that the crystallinity of the COF can be improved by increasing the planarity of the linkage monomers, which is consistent with our results.[47] The most planar monomers, TPT-3NH$_2$ and TPT-3CHO, produced TPT-COF-6, which possessed the largest value of d_{100} (2.19 nm) and the shortest interlayer distance (3.48

Table 2 PXRD and BET parameters of the synthesized COFs

	d_{100} (nm)	Pore size (nm)	S_{BET} (m² g⁻¹)	$S_{Langmuir}$ (m² g⁻¹)	Pore vol. (cm³ g⁻¹)
TPA-COF-1	1.75	1.93	714	1058	0.517
TPA-COF-2	1.90	1.80	478	704	0.333
TPA-COF-3	1.91	2.01	557	823	0.353
TPT-COF-4	1.91	2.13	1132	1657	0.767
TPT-COF-5	2.18	2.50	1747	2617	1.102
TPT-COF-6	2.19	2.55	1535	2456	1.019

Å); in contrast, the least planar monomers—TPA-3NH₂ and TPA-3CHO—produced TPA-COF-1, which featured the lowest value of d_{100} (1.75 nm) and the longest interlayer distance (4.40 Å). The permanent porosity of the TPA-COFs and TPT-COFs was demonstrated by measuring their N₂ sorption at 77 K. As presented in Fig. 3, the sorption curves of all of the COFs displayed the type I isothermal behavior that is characteristic of microporous polymers. Interestingly, the Brunauer–Emmett–Teller (BET) and Langmuir surface areas of the symmetrical and unsymmetrical COFs were strongly affected by the planarity of the monomers. Thus, while the PXRD data revealed an increasing degree of crystallinity upon increasing the planarity of the monomers, we observed a further demarcation in the BET and Langmuir surface areas of the COFs. In the case of the symmetrical monomers, the BET surface area of the TPT–TPT-COF (TPT-COF-6), produced from the symmetrical and most planar TPT-3NH₂ and TPT-3CHO monomers, was 1535 m² g⁻¹, significantly higher than that (714 m² g⁻¹) of the TPA–TPA-COF (TPA-COF-1), obtained from the symmetrical and least planar TPA-3NH₂ and TPA-3CHO monomers. On the other hand, when using unsymmetrical monomers (Table 2), the TPA–TPP-COF (TPA-COF-2), prepared from the least planar TPP-3CHO monomer, exhibited a lower BET surface area (478 m² g⁻¹) than the TPA–TPT-COF (TPA-COF-3, 557 m² g⁻¹), prepared from the most planar TPT-3CHO monomer (Table 2). Likewise, the TPT–TPA-COF (TPT-COF-4) featured a BET surface area (1132 m² g⁻¹)

lower than that (1747 m² g⁻¹) of the TPT–TPP-COF (TPT-COF-5). In addition, the Langmuir surface area of these COFs showed the same findings; the TPT–TPT-COF (TPT-COF-6) exhibited a Langmuir surface area (2456 m² g⁻¹) higher than that (1058 m² g⁻¹) of the TPA–TPA-COF (TPA-COF-1), the TPA–TPP-COF (TPA-COF-2) showed a lower Langmuir surface area (704 m² g⁻¹) than the TPA–TPT-COF (TPA-COF-3, 823 m² g⁻¹), and the TPT–TPA-COF (TPT-COF-4) exhibited a Langmuir surface area (1657 m² g⁻¹) lower than that (2617 m² g⁻¹) of the TPT–TPP-COF (TPT-COF-5).

These data indicate that two main factors affected the BET and Langmuir surface areas of the COFs: symmetry and planarity. For the symmetrical COFs, lowering the planarity of the monomers induced a lower surface area; similarly for the unsymmetrical COFs, lowering the planarity of the monomers led to a lower surface area.

We used the nonlocal density functional theory method to calculate the pore size distributions of the COFs. The TPA-COFs—TPA–TPA-COF (TPA-COF-1), TPA–TPP-COF (TPA-COF-2), and TPA–TPT-COF (TPA-COF-3)—were microporous materials having pore sizes of 1.93, 1.80, and 2.01 nm, respectively. On the other hand, the TPT-COFs—TPT–TPA-COF (TPT-COF-4), TPT–TPP-COF (TPT-COF-5), and TPT–TPT-COF (TPT-COF-6)—were sort of mesoporous materials having pore sizes of 2.13, 2.50, and 2.55 nm, respectively (Fig. 4 and Table 2).

We observed the surface morphologies of the six COFs through scanning electron microscopy (SEM, Fig. S30†). The
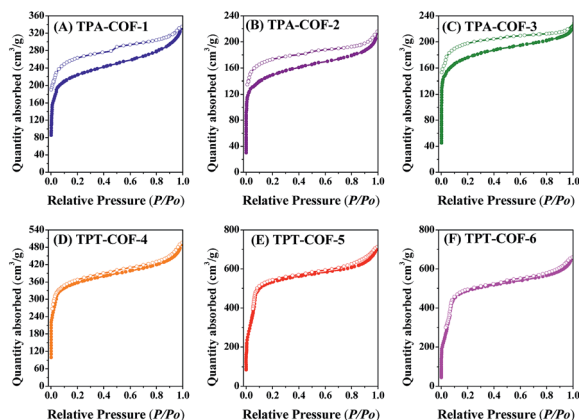

Fig. 3 N₂ adsorption (●, filled cycles) and desorption (○, open cycles) isotherms, measured at 298 K, of the TPA-COFs: (A) TPA–TPA-COF (TPA-COF-1), (B) TPA–TPP-COF (TPA-COF-2), and (C) TPA–TPT-COF (TPA-COF-3), and the TPT-COFs: (D) TPT–TPA-COF (TPT-COF-4), (E) TPT–TPP-COF (TPT-COF-5), and (F) TPT–TPT-COF (TPT-COF-6).

Fig. 4 Pore size distribution profiles of the TPA-COFs: (A) TPA–TPA-COF (TPA-COF-1), (B) TPA–TPP-COF (TPA-COF-2), and (C) TPA–TPT-COF (TPA-COF-3), and the TPT-COFs: (D) TPT–TPA-COF (TPT-COF-4), (E) TPT–TPP-COF (TPT-COF-5), and (F) TPT–TPT-COF (TPT-COF-6).
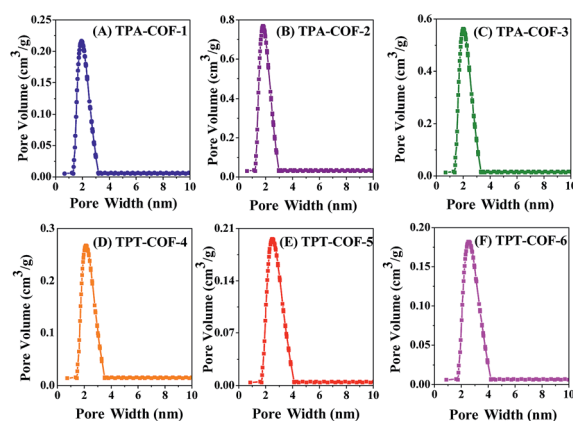
This journal is © The Royal Society of Chemistry 2018

J. Mater. Chem. A, 2018, **6**, 19532–19541 | **19537**

SEM images of the TPA–TPA-COF (TPA-COF-1) and TPA–TPP-COF (TPA-COF-2) revealed homogeneous assemblies of loose agglomerates of very small particles having irregular shapes (Fig. S30A and B†), while those of the TPT–TPA-COF (TPT-COF-4) and TPT–TPP-COF (TPT-COF-5) revealed chip-like morphologies of micrometer dimensions (Fig. S30D and E†). Interestingly, the TPA–TPT-COF (TPA-COF-3) and TPT–TPT-COF (TPT-COF-6) exhibited rod-like morphologies as well as agglomerates of tiny particles (Fig. S30C and F†).

We examined the degrees of CO_2 adsorption of each series particularly: TPA-COFs and TPT-COFs at temperatures of 298 and 273 K (Fig. 5). The nitrogen content and nitrogen nucleophilicity strongly affect the CO_2 uptake efficiency of the prepared COFs. For the TPA-COFs series, the TPA–TPT-COF (TPA-COF-3), which we had prepared from the highest-nitrogen-content TPT-3CHO monomer, exhibited the highest CO_2 uptake capacities: 63.94 and 91.15 mg g^{-1} at 298 and 273 K, respectively. The TPA–TPP-COF (TPA-COF-2), featuring three triarylamine and three triarylpyridine units in each hexagonal pore, displayed CO_2 uptake capacities of 45.88 and 82.42 mg g^{-1} at 298 and 273 K, respectively. These capacities are 1.2-fold higher than those of the TPA–TPA-COF (TPA-COF-1) with six triarylamine units in the hexagonal pore. The nitrogen content in the TPA–TPA-COF (TPA-COF-1) and TPA–TPP-COF (TPA-COF-2) is similar. Therefore, the enhanced CO_2 uptake efficiency of the TPA–TPP-COF (TPA-COF-2) over the TPA–TPA-COF (TPA-COF-1) was presumably due to the steric hindrance around the nitrogen atom in the non-planar triarylamine unit being more than that in the planar triarylpyridine unit. As the steric hindrance around the nitrogen atom increased, the nucleophilicity of the nitrogen atom decreased and thus the number of adsorbed carbon dioxide molecules also decreased.[48] Similarly, for the TPT-COF series, the TPT–TPT-COF (TPT-COF-6), having six triaryltriazine units in its hexagonal pore, provided the highest CO_2 uptake capacities: 65.65 and 92.38 mg g^{-1} at 298 and 273 K, respectively. The TPT–TPP-COF (TPT-COF-5) exhibited CO_2 uptake capacities of 41.00 and

59.44 mg g^{-1} at 298 and 273 K, respectively. These capacities are 1.1-fold higher than those of the TPT–TPA-COF (TPT-COF-4). Thus, increases in the nitrogen content and nitrogen nucleophilicity of the monomer led to an increase in the CO_2 uptake capacity of the COF. We observed the same phenomena for both the TPA-COF and TPT-COF series.

To support these observations, we calculated the isosteric heat of adsorption (Q_{st}) from the CO_2 adsorption data measured at 298 and 273 K, according to the Clausius–Clapeyron equation. Fig. S31–S36† shows the fitting isotherms of each COF which indicated that at a low loading of CO_2 (0.1 mmol g^{-1}, as the standard), the TPA–TPA-COF (TPA-COF-1), TPA–TPP-COF (TPA-COF-2), and TPA–TPT-COF (TPA-COF-3) provided values of Q_{st} of 15.92, 25.88, and 28.11 kJ mol^{-1}, respectively; for the TPT–TPA-COF (TPT-COF-4), TPT–TPP-COF (TPT-COF-5), and TPT–TPT-COF (TPT-COF-6), these values were 9.70, 16.97, and 30.59 kJ mol^{-1}, respectively. The trends in these values of Q_{st} reveal that the incorporation of higher-nitrogen-content triaryltriazine units into the backbones of the TPA-COFs and TPT-COFs encouraged stronger interactions with CO_2. On the other hand, the value of Q_{st} for the TPA–TPA-COF (TPA-COF-1) was lower than that of the TPA–TPP-COF (TPA-COF-2), and for the TPT–TPA-COF (TPT-COF-4) it was lower than that of the TPT–TPP-COF (TPT-COF-5), confirming that the incorporation of the more nucleophilic triarylpyridine units into the backbones of COFs enhanced the quadrupolar interactions with CO_2.

Next, we examined the redox activity of the COFs containing triphenylamine groups in the backbones (highlighted in red in their chemical structures, Fig. 6). Generally, triphenylamine groups are redox-active units that can store electrochemical energy.[49,50] Among our six samples, the COFs-1–4 featured
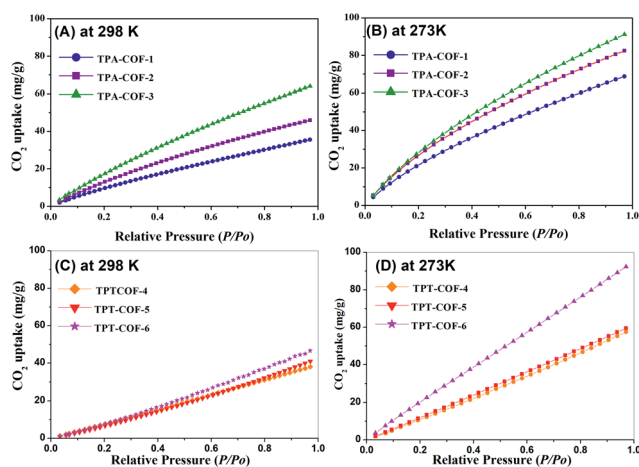

Fig. 5 CO_2 uptake profiles of (A and B) the TPA-COFs: TPA–TPA-COF (TPA-COF-1), TPA–TPP-COF (TPA-COF-2), and TPA–TPT-COF (TPA-COF-3), and (C and D) the TPT-COFs: TPT–TPA-COF (TPT-COF-4), TPT–TPP-COF (TPT-COF-5), and TPT–TPT-COF (TPT-COF-6), measured at (A and C) 298 K and (B and D) 273 K.
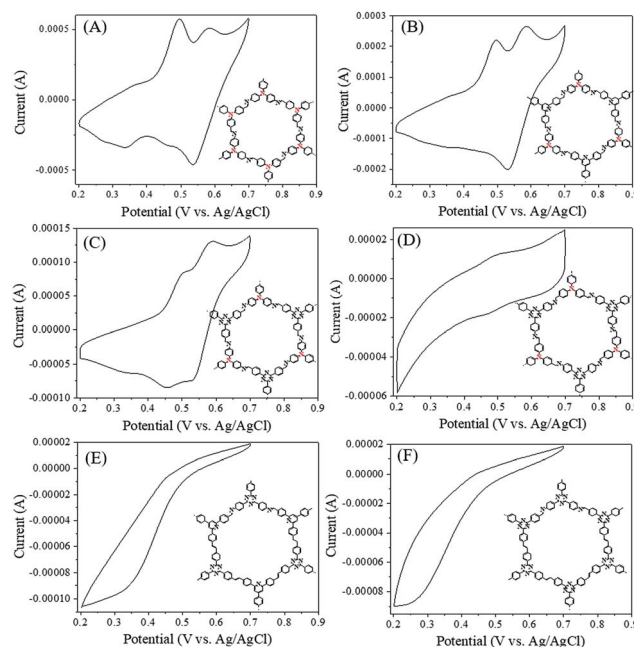

Fig. 6 Cyclic voltammograms of the COFs measured at 5 mV s^{-1}: (A) TPA-COF-1, (B) TPA-COF-2, (C) TPA-COF-3, (D) TPT-COF-4, (E) TPT-COF-5, and (F) TPT-COF-6.

19538 | J. Mater. Chem. A, 2018, 6, 19532–19541

This journal is © The Royal Society of Chemistry 2018

triphenylamine groups. Cyclic voltammetry (CV) revealed the redox behavior of the COFs-1–4, with reversible redox processes occurring in a potential window of 0.2–0.7 V (Fig. 6A–D and S37A–D†). In contrast, no redox peaks appeared in the CV traces of TPT-COF-5 and TPT-COF-6 (Fig. 6E, F and S37E, F†) because their unsaturated N=C units were unreactive in the presence of H^+ (from the H_2SO_4 electrolyte), in contrast to the higher basicity of C–NH–C units.[51] To test their suitability for use as pseudocapacitors, we calculated the specific capacitances of all of our samples from the galvanostatic charge/discharge (GCD) data (Fig. 7). Fig. 8 presents the specific capacitances of these COFs. Although TPT-COF-5 and TPT-COF-6 had high surface areas, they displayed very small specific capacitances, due to the absence of redox-active groups. Notably, the specific capacitances were enhanced upon increasing the number of triphenylamine groups. For example, TPA–TPA-COF-1 has six triphenylamine groups, while the COFs-2–4 have three; TPA–TPA-COF-1 exhibited the highest specific capacitance of 51.3 F g^{-1} at 0.2 A g^{-1} which is a value higher than that of 28 F g^{-1} at 0.2 A g^{-1} for a previously reported β-ketoenamine-based 2D COF.[52] Although the COFs-2–4 all featured three triphenylamine groups, their specific capacitances were 14.4, 5.1, and 2.4 F g^{-1}, respectively, at 0.2 A g^{-1}. From these results, we conclude that redox-active groups are an important factor affecting the capacitance, but porosity control is also critical when designing COFs for use as supercapacitors.

Conclusions

We have synthesized two series of highly crystalline and high-surface-area COFs (TPA-COFs and TPT-COFs) based on Schiff base polycondensations of triarylamines and trialdehydes having various nitrogen contents and degrees of planarity and symmetry. We elucidated the chemical structures of these COFs using FTIR spectroscopy, elemental analysis, and solid state ^{13}C NMR spectroscopy. Thermal analyses of these six TPA-COFs and TPT-COFs revealed that they were thermally stable at temperatures up to 509–553 °C. The symmetry, planarity, and nitrogen content of the monomers all played roles impacting the crystallinity, BET surface area, and CO_2 uptake of the COFs. For example, when using symmetrical monomers, the TPT–TPT-COF (TPT-COF-6), prepared from the most planar monomers, exhibited a BET surface area of 1535.3 m^2 g^{-1}, significantly higher than that of the TPA–TPA-COF (TPA–TPA-COF-1), produced from the least planar monomers; when using unsymmetrical monomers, the TPA–TPP-COF (TPA-COF-2), prepared from the least planar TPP-3CHO monomer, provided a BET surface area of 478.1 m^2 g^{-1} that was lower than that of the TPA–TPT-COF (TPA-COF-3), prepared from the more planar TPT-3CHO monomer. Because some of the synthesized COFs possessed redox-active triphenylamine groups, we tested them for application in electrochemical storage. The TPA–TPA-COF-1 exhibited the highest specific capacitance (51.3 F g^{-1} at 0.2 A g^{-1}) among our six COFs, consistent with its greater number of redox-active groups in the COF unit structure. We also found that a greater content of micropores decreased the specific capacitance when the COFs had the same number of redox-active groups. This study not only emphasizes the importance of monomer symmetry and planarity in the crystallinity of the resultant COFs but also exposes the impact of these features on CO_2 uptake and, hence, environmental applications. In addition, it appears that COFs containing redox-active groups might be suitable for application in energy storage systems.
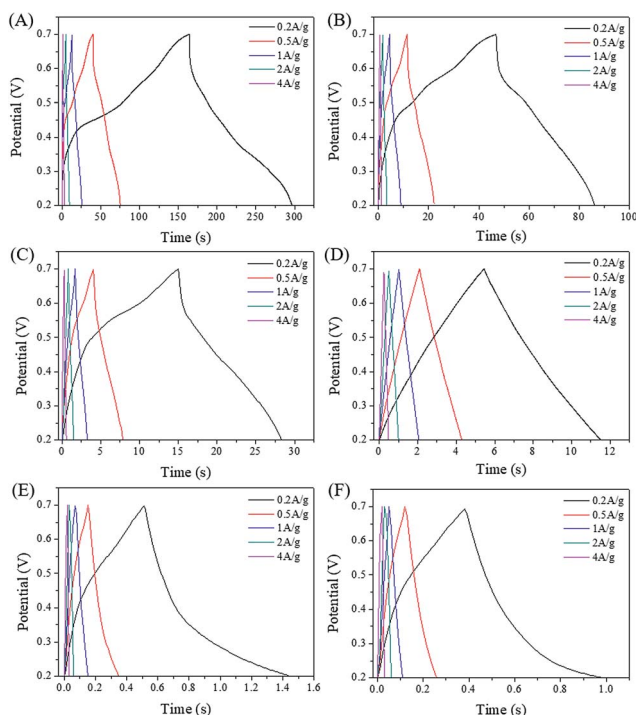

Fig. 7 Galvanostatic charge/discharge curves of the COFs measured at various current densities: (A) TPA-COF-1, (B) TPA-COF-2, (C) TPA-COF-3, (D) TPT-COF-4, (E) TPT-COF-5, and (F) TPT-COF-6.
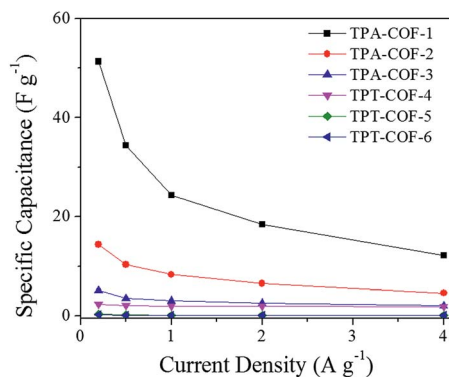

Fig. 8 Specific capacitances of the COFs determined from galvanostatic charge/discharge data at various current densities.

Conflicts of interest

There are no conflicts to declare.

Acknowledgements

Notes and references

1 S. Y. Ding and W. Wang, *Chem. Soc. Rev.*, 2013, **42**, 548–568.
2 X. Feng, X. Ding and D. Jiang, *Chem. Soc. Rev.*, 2012, **41**, 6010–6022.
3 H. L. Qian, C. X. Yang and X. P. Yan, *Nat. Commun.*, 2016, **7**, 12104.
4 H. M. El-Kaderi, J. R. Hunt, J. L. Mendoza-Cortés, A. P. Côté, R. E. Taylor, M. O'Keeffe and O. M. Yaghi, *Science*, 2007, **316**, 268–272.
5 J. T. Yu, Z. Chen, J. Sun, Z. T. Huang and Q. Y. Zheng, *J. Mater. Chem.*, 2012, **22**, 5369–5373.
6 Q. Fang, Z. Zhuang, S. Gu, R. B. Kaspar, J. Zheng, J. Wang, S. Qiu and Y. Yan, *Nat. Commun.*, 2014, **5**, 4503.
7 H. Furukawa and O. M. Yaghi, *J. Am. Chem. Soc.*, 2009, **131**, 8875–8883.
8 G. Das, B. P. Biswal, S. Kandambeth, V. Venkatesh, G. Kaur, M. Addicoat, T. Heine, S. Vermab and R. Banerjee, *Chem. Sci.*, 2015, **6**, 3931–3939.
9 S. Dalapati, S. Jin, J. Gao, Y. Xu, A. Nagai and D. Jiang, *J. Am. Chem. Soc.*, 2013, **135**, 17310–17313.
10 S. Y. Ding, M. Dong, Y. W. Wang, Y. T. Chen, H. Z. Wang, C. Y. Su and W. Wang, *J. Am. Chem. Soc.*, 2016, **138**, 3031–3037.
11 S. Wan, J. Guo, J. Kim, H. Ihee and D. Jiang, *Angew. Chem., Int. Ed.*, 2009, **48**, 5439–5442.
12 Y. Wu, H. Xu, X. Chen, J. Gao and D. Jiang, *Chem. Commun.*, 2015, **51**, 10096–10098.
13 S. Y. Ding, J. Gao, Q. Wang, Y. Zhang, W. G. Song, C. Y. Su and W. Wang, *J. Am. Chem. Soc.*, 2011, **133**, 19816–19822.
14 H. S. Xu, S. Y. Ding, W. K. An, H. Wu and W. Wang, *J. Am. Chem. Soc.*, 2016, **138**, 11489–11492.
15 S. Lin, C. S. Diercks, Y. B. Zhang, N. Kornienko, E. M. Nichols, Y. Zhao, A. R. Paris, D. Kim, P. Yang, O. M. Yaghi and C. J. Chang, *Science*, 2015, **349**, 1208–1213.
16 H. Xu, J. Gao and D. Jiang, *Nat. Chem.*, 2015, **7**, 905–912.
17 S. Kandambeth, B. P. Biswa, H. D. Chaudhari, K. C. Rout, S. H. Kunjattu, S. Mitra, S. Karak, A. Das, R. Mukherjee, U. K. Kharu and R. Banerjee, *Adv. Mater.*, 2017, **29**, 1–9.
18 Q. Sun, B. Aguila, J. Perman, L. D. Ear, C. W. Abney, Y. Cheng, H. Wei, N. Nguyen, L. Wojtas and S. Ma, *J. Am. Chem. Soc.*, 2017, **139**, 2786–2793.
19 F. Xu, S. Jin, H. Zhong, D. Wu, X. Yang, X. Chen, H. Wei, R. Fu and D. Jiang, *Sci. Rep.*, 2015, **5**, 8225.
20 C. R. DeBlase, K. E. Silberstein, T. T. Truong, H. D. Abruña and W. R. Dichtel, *J. Am. Chem. Soc.*, 2013, **135**, 16821–16824.

21 L. Bai, Q. Gao and Y. Zhao, *J. Mater. Chem. A*, 2016, **4**, 14106–14110.
22 J. Kim, J. H. Kim and K. Ariga, *Joule*, 2017, **1**, 739–768.
23 S. Mitra, H. S. Sasmal, T. Kundu, S. Kandambeth, K. Illath, D. D. Díaz and R. Banerjee, *J. Am. Chem. Soc.*, 2017, **139**, 4513–4520.
24 Q. Fang, J. Wang, S. Gu, R. B. Kaspar, Z. Zhuang, J. Zheng, H. Guo, S. Qiu and Y. Yan, *J. Am. Chem. Soc.*, 2015, **137**, 8352–8355.
25 L. Bai, S. Z. F. Phua, W. Q. Lim, A. Jana, Z. Luo, H. P. Tham, L. Zhao, Q. Gao and Y. Zhao, *Chem. Commun.*, 2016, **52**, 4128–4131.
26 S. Wan, F. Gándara, A. Asano, H. Furukawa, A. Saeki, S. K. Dey, L. Liao, M. W. Ambrogio, Y. Y. Botros, X. Duan, S. Seki, J. F. Stoddart and O. M. Yaghi, *Chem. Mater.*, 2011, **23**, 4094–4097.
27 A. P. Côté, A. I. Benin, N. W. Ockwig, M. O'Keeffe, A. J. Matzger and O. M. Yaghi, *Science*, 2005, **310**, 1166–1170.
28 X. Ding, J. Guo, X. Feng, Y. Honsho, J. Guo, S. Seki, P. Maitarad, A. Saeki, S. Nagase and D. Jiang, *Angew. Chem., Int. Ed.*, 2011, **50**, 1289–1293.
29 F. J. Uribe-Romo, J. R. Hunt, H. Furukawa, C. Klöck, M. O'Keeffe and O. M. Yaghi, *J. Am. Chem. Soc.*, 2009, **131**, 4570–4571.
30 G. Das, D. B. Shinde, S. Kandambeth, B. P. Biswal and R. Banerjee, *Chem. Commun.*, 2014, **50**, 12615–12618.
31 X. Chen, M. Addicoat, S. Irle, A. Nagai and D. Jiang, *J. Am. Chem. Soc.*, 2013, **135**, 546–549.
32 P. Kuhn, M. Antonietti and A. Thomas, *Angew. Chem., Int. Ed.*, 2008, **47**, 3450–3453.
33 S. Hug, M. B. Mesch, H. Oh, N. Popp, M. Hirscher, J. Senkerd and B. V. Lotsch, *J. Mater. Chem. A*, 2014, **2**, 5928–5936.
34 X. Feng, X. Ding and D. Jiang, *Chem. Soc. Rev.*, 2012, **41**, 6010–6022.
35 J. L. Segura, M. J. Mancheño and F. Zamora, *Chem. Soc. Rev.*, 2016, **45**, 5635–5671.
36 Y. Peng, W. K. Wong, Z. Hu, Y. Cheng, D. Yuan, S. A. Khan and D. Zhao, *Chem. Mater.*, 2016, **28**, 5095–5101.
37 T. Y. Zhou, S. Q. Xu, Q. Wen, Z. F. Pang and X. Zhao, *J. Am. Chem. Soc.*, 2014, **136**, 15885–15888.
38 Z. F. Pang, S. Q. Xu, T. Y. Zhou, R. R. Liang, T. G. Zhan and X. Zhao, *J. Am. Chem. Soc.*, 2016, **138**, 4710–4713.
39 S. Karak, S. Kandambeth, B. P. Biswal, H. S. Sasmal, S. Kumar, P. Pachfule and R. Banerjee, *J. Am. Chem. Soc.*, 2017, **139**, 1856–1862.
40 S. Kandambeth, D. B. Shinde, M. K. Panda, B. Lukose, T. Heine and R. Banerjee, *Angew. Chem., Int. Ed.*, 2013, **52**, 13052–13056.
41 F. Auras, L. Ascherl, A. H. Hakimioun, J. T. Margraf, F. C. Hanusch, S. Reuter, D. Bessinger, M. Döblinger, C. Hettstedt, K. Karaghiosoff, S. Herbert, P. Knochel, T. Clark and T. Bein, *J. Am. Chem. Soc.*, 2016, **138**, 16703–16710.
42 L. Ascher, T. Sick, J. T. Margraf, S. H. Lapidus, M. Calik, C. Hettstedt, K. Karaghiosoff, M. Döblinger, T. Clark, K. W. Chapman, F. Auras and T. Bein, *Nat. Chem.*, 2016, **8**, 310–316.

43 A. Halder, S. Kandambeth, B. P. Biswa, G. Kaur, N. C. Roy, M. Addicoat, J. K. Salunke, S. Banerjee, K. Vanka, T. Heine, S. Verma and R. Banerjee, *Angew. Chem., Int. Ed.*, 2016, **55**, 7806–7810.

44 Q. Gao, X. Li, G. H. Ning, H. S. Xu, C. Liu, B. Tian, W. Tang and K. P. Loh, *Chem. Mater.*, 2018, **30**, 1762–1768.

45 F. Haase, K. Gottschling, L. Stegbauer, L. S. Germann, R. Gutzler, V. Duppel, V. S. Vyas, K. Kern, R. E. Dinnebier and B. V. Lotsch, *Mater. Chem. Front.*, 2017, **1**, 1354–1361.

46 L. Zhai, N. Huang, H. Xu, Q. Chen and D. Jiang, *Chem. Commun.*, 2017, **53**, 4242–4245.

47 J. Dong, Y. Wang, G. Liu, Y. Cheng and D. Zhao, *CrystEngComm*, 2017, **19**, 4899–4909.

48 P. V. Kortunov, M. Siskin, M. Paccagnini and H. Thomann, *Energy Fuels*, 2016, **30**, 1223–1236.

49 C. Su, F. Yang, L. Ji, L. Xu and C. Zhang, *J. Mater. Chem. A*, 2014, **2**, 20083–20088.

50 C. Su, H. He, L. Xu, K. Zhao, C. Zheng and C. Zhang, *J. Mater. Chem. A*, 2017, **5**, 2701–2709.

51 A. M. Khattak, Z. A. Ghazi, B. Liang, N. Ali Khan, A. Iqba, L. Li and Z. Tang, *J. Mater. Chem. A*, 2016, **4**, 16312–16317.

52 C. R. DeBlase, K. E. Silberstein, T. T. Truong, H. D. Abruña and W. R. Dichtel, *J. Am. Chem. Soc.*, 2013, **135**, 16821–16824.